

See discussions, stats, and author profiles for this publication at: <https://www.researchgate.net/publication/41030386>

Investigation of the Mechanism of Colloidal Silicalite-1 Crystallization by Using DLS, SAXS, and ^{29}Si NMR Spectroscopy

ARTICLE in CHEMISTRY - A EUROPEAN JOURNAL · MARCH 2010

Impact Factor: 5.73 · DOI: 10.1002/chem.200901688 · Source: PubMed

CITATIONS

40

READS

262

9 AUTHORS, INCLUDING:



Alexander Aerts

Belgian Nuclear Research Centre

55 PUBLICATIONS 945 CITATIONS

SEE PROFILE



Titus S. van Erp

Norwegian University of Science and Techno...

59 PUBLICATIONS 1,092 CITATIONS

SEE PROFILE



Jan Vermant

ETH Zurich

162 PUBLICATIONS 4,611 CITATIONS

SEE PROFILE



Christine E A Kirschhock

University of Leuven

229 PUBLICATIONS 4,432 CITATIONS

SEE PROFILE

Investigation of Nanoparticles Occurring in the Colloidal Silicalite-1 Zeolite Crystallization Process Using Dissolution Experiments

Tom P. Caremans,[†] Benoit Loppinet,[‡] Lana R. A. Follens,[†] Titus S. van Erp,[†] Jan Vermant,[§] Bart Goderis,^{||} Christine E. A. Kirschhock,^{*,†} Johan A. Martens,[†] and Alexander Aerts[‡]

[†]Centre for Surface Chemistry and Catalysis, Department M2S, K.U. Leuven, Kasteelpark Arenberg 23, 3001 Heverlee, Belgium, [‡]FORTH, Institute of Electronic Structure & Laser, P.O. Box 1527, 71110, Heraklion, Crete, Greece, [§]Laboratory of Applied Rheology and Polymer Processing, Department of Chemical Engineering, K.U. Leuven, W. de Croylaan 46, 3001 Heverlee, Belgium, and

^{||}Chemistry Department, Molecular and Nanomaterials Division, K.U. Leuven, Celestijnenlaan 200F, 3001 Heverlee, Belgium

Received July 29, 2009. Revised Manuscript Received April 23, 2010

In concentrated clear sol prepared from tetraethylorthosilicate, tetrapropylammonium hydroxide, and water suitable for crystallization of Silicalite-1 zeolite, the main part of the silica is present in nanoparticles. The nature of these nanoparticles and their evolution during the induction period and the stage of early crystal growth was investigated via dissolution experiments in the presence of excess TPAOH. The dissolution process was monitored *in situ* using static and dynamic light scattering (SLS/DLS) and synchrotron small-angle X-ray scattering (SAXS). The complete dissolution of an individual nanoparticle was observed to occur in one step. Dissolution transformed a nanoparticle into a cluster of silicate oligomers. Larger grown nanoparticles dissolved slower. Exponential dissolution rate constants scaled inversely proportional with the volume of the nanoparticle's silica core. This experimentally observed dissolution behavior was modeled by assuming that a nanoparticle dissolved to oligomers via a series of partially dissolved nanoparticles that correspond to metastable intermediate states of increasing free energy. The resulting free energy barrier that has to be overcome by a dissolving nanoparticle could be derived from the experimental input. The idealized free energy profile provided a qualitative explanation for the apparent instantaneous disintegration of entire nanoparticles.

Introduction

Zeolites are technical materials designed for application in various domains such as heterogeneous catalysis,^{1,2} pollution abatement,^{3–5} and sensors.^{6,7} Silicalite-1 is an all-silica zeolite with MFI framework topology that can be synthesized from a clear sol.⁸ The optically transparent clear sol is obtained upon the reaction of tetraethyl orthosilicate (TEOS) in an aqueous solution of tetrapropylammonium hydroxide (TPAOH). When this mixture is heated, Silicalite-1 crystallizes within a time frame of hours. In the clear sol, silica speciation is complicated. Besides the dissolved silicate monomer and oligomers, the sol contains nanoparticles. These nanoparticles adopt specific sizes

(2–10 nm) and various internal silicate connectivities depending on conditions.^{9,10} Their internal structure is difficult to determine. They appear amorphous in XRD and do not show lattice spacings in electron microscopy. On the basis of indirect experimental evidence, the internal structure of the nanoparticles has been described in different ways. The models differ essentially with respect to the specificity of the silicate connectivity and the occlusion of TPA. Description in terms of *amorphous* versus *crystalline* is less appropriate in a discussion of the properties of these small silicate nanoparticles. The term *structured* will be used here to refer to the development of a tridimensional silicate network with zeolite-specific loop configurations.¹¹

Some authors proposed the nanoparticles to be merely the silicate source providing dissolved oligomers and monomers for crystal growth.^{12,13} Others, including some of us, attributed a more prominent role to the nanoparticles, and

*Corresponding author. E-mail: christine.kirschhock@biw.kuleuven.be.

- (1) Davis, R. J. *J. Catal.* **2003**, 216, 396.
- (2) Clerici, M. G. *Top. Catal.* **2000**, 13, 373.
- (3) Panayotova, M. I. *Waste Manage.* **2001**, 21, 671.
- (4) Yeom, Y. H.; Wen, B.; Sachtler, W. M. H.; Weitz, E. *J. Phys. Chem. B* **2004**, 108, 5386.
- (5) Brandenberger, S.; Krocher, O.; Tissler, A.; Althoff, R. *Cat. Rev. Sci. Eng.* **2008**, 50, 492.
- (6) Rauch, W. L.; Liu, M. J. *Mater. Sci.* **2003**, 38, 4307.
- (7) Mintova, S.; Mo, S. Y.; Bein, T. *Chem. Mater.* **2001**, 13, 901.
- (8) Persson, A. E.; Schoeman, B. J.; Sterte, J.; Otterstedt, J. E. *Zeolites* **1994**, 14, 557.
- (9) Aerts, A.; Follens, L. R. A.; Haouas, M.; Caremans, T. P.; Delsuc, M.-A.; Loppinet, B.; Vermant, J.; Goderis, B.; Taulelle, F.; Martens, J. A.; Kirschhock, C. E. A. *Chem. Mater.* **2007**, 19, 3448–3454.

- (10) Follens, L. R. A.; Aerts, A.; Haouas, M.; Caremans, T. P.; Loppinet, B.; Goderis, B.; Vermant, J.; Taulelle, F.; Martens, J. A.; Kirschhock, C. E. A. *Phys. Chem. Chem. Phys.* **2008**, 10, 5574.
- (11) Baerlocher, C.; McCusker, L. B.; Olson, D. H. *Atlas of Zeolite Framework Types*, 6th ed.; Elsevier: Amsterdam, The Netherlands, 2007.
- (12) Schoeman, B. J. *Microporous Mesoporous Mater.* **1998**, 22, 9.
- (13) Cundy, C. S.; Cox, P. A. *Microporous Mesoporous Mater.* **2005**, 82, 1.

proposed their involvement in an oriented aggregation process.^{14–17} De Moor et al.,¹⁸ Burkett et al.,^{19,20} and Hsu et al.²¹ postulated that the nanoparticles occluded TPA and had some initial ordering, but zeolitic internal structuring according to those authors was reached only after aggregation. In more recent aggregative growth models, aggregation is believed to proceed selectively from the most structured nanoparticles that exist in small concentration in the clear sol.^{22–24} In such kinetic models, the internal structure of the nanoparticles is assumed to improve progressively, thus increasing the probability for involvement in aggregation processes contributing to crystal growth. The structural evolution of the nanoparticles is a time limiting factor in such aggregative growth processes. The formation of fully structured nanoparticles with TPA molecules occluded in channel intersections has been proposed in the nanoslab model,^{25–27} which has been discussed controversially.^{28–30} Because of its nanodimensions, the zeolitic network in a nanoslab does not immediately reach the permanence and stiffness of a zeolite crystal but transforms into increasingly stable silicate species over time. The evolution toward more zeolite-like connectivity was deduced from the shifting of the fingerprint IR absorption band with the size of the MFI fragment.³¹ In the latest formulation of the model, it was proposed that only part of the nanoparticles, namely, those with a condensed zeolite-like framework, evolve into building blocks for Silicalite-1 nucleation and growth.³²

Several experimental techniques have been used to monitor the size and the internal structure of the nanoparticles during Silicalite-1 crystallization. Pioneered by Schoeman and co-workers,³³ dynamic light scattering was used for simultaneous detection of nanoparticles and growing crystals at hydrothermal conditions.^{21,34} During the induction stage of the crystallization, the size of the nanoparticles slightly increases.^{32,35} This process was found to be irreversible upon cooling.³⁶ Also during induction, infrared and ²⁹Si NMR spectroscopy revealed that the silicate connectivity of the nanoparticle framework increased.^{32,37,38} The onset of crystal growth was marked by a sudden jump of the effective diameter measured by DLS.³⁵ At this stage, small-angle X-ray scattering (SAXS) patterns evidenced the formation of a low concentration of larger particles (~10 nm) next to the nanoparticles.³⁹ Cryo-transmission electron microscopy (cryo-TEM) revealed the presence of ~10 nm particles with crystal lattice spacings.¹⁷ These early crystals had an aggregate-like morphology with crystalline domain sizes similar to the size of nanoparticles,^{17,22,24} supporting the model of crystal formation through an oriented aggregation mechanism.

Disturbing the sol by dilution, changing alkalinity, or cooling is an alternative approach that has been used to investigate the properties of the nanoparticles. In a recent study, the dissolution of nanoparticles was investigated, after increasing the sol alkalinity by adding extra TPAOH.⁴⁰ With increasing hydrothermal treatment time, the nanoparticles showed increasing resistance toward dissolution. Nanoparticle dissolution rates and enthalpies evolved toward the values for Silicalite-1 crystals, and it was concluded that the nanoparticles exhibit an internal reorganization toward a material that is more zeolite-like in structure.⁴⁰ A model originally developed for nanoparticle growth was found to give a reasonable description of the dissolution process.³⁸ This model was based on the assumption that nanoparticle growth and fragmentation occurs via addition or subtraction of silicate monomers.

The investigation of zeolitic nanoparticle dissolution thus provides insight into their formation and their structural evolution during crystallization. Previous studies of nanoparticle dissolution were performed on dilute clear sols (TEOS/TPAOH/H₂O of Y:X:9500) with Y varying between 40 and 80, and X between 4.5 and 27).⁴⁰ In the present work, we investigated more concentrated sols with molar

- (14) Dokter, W. H.; Van Garderen, H. F.; Beelen, T. P. M.; van Santen, R. A.; Bras, W. *Angew. Chem., Int. Ed. Engl.* **1995**, *34*, 73.
- (15) Watson, J. N.; Iton, L. E.; Keir, R. I.; Thomas, J. C.; Dowling, T. L.; White, J. W. *J. Phys. Chem. B* **1997**, *101*, 10094.
- (16) Houssin, C. J. Y.; Kirschhock, C. E. A.; Magusin, P. C. M. M.; Mojet, B. L.; Grobet, P. J.; Jacobs, P. A.; Martens, J. A.; van Santen, R. A. *Phys. Chem. Chem. Phys.* **2003**, *5*, 3518–3524.
- (17) Kumar, S.; Davis, T. M.; Ramanan, H.; Penn, R. L.; Tsapatsis, M. *J. Phys. Chem. B* **2007**, *111*, 3398.
- (18) de Moor, P. P. E. A.; Beelen, T. P. M.; Komanschek, B. U.; Beck, L. W.; Wagner, P.; Davis, M. E.; van Santen, R. A. *Chem.—Eur. J.* **1999**, *5*, 2083.
- (19) Burkett, S. L.; Davis, M. E. *Chem. Mater.* **1995**, *7*, 920.
- (20) Burkett, S. L.; Davis, M. E. *Chem. Mater.* **1995**, *7*, 1453.
- (21) Hsu, C.-Y.; Chiang, A. S. T.; Selvin, R.; Thompson, R. W. *J. Phys. Chem. B* **2005**, *109*, 18804.
- (22) Davis, T. M.; Drews, T. O.; Ramanan, H.; He, C.; Dong, J.; Schnablegger, H.; Katsoulakis, M. A.; Kokkoli, E.; McCormick, A. V.; Penn, R. L.; Tsapatsis, M. *Nat. Mater.* **2006**, *5*, 400.
- (23) Snyder, M. A.; Tsapatsis, M. *Angew. Chem., Int. Ed.* **2007**, *46*, 7560.
- (24) Kumar, S.; Wang, Z.; Penn, R. L.; Tsapatsis, M. *J. Am. Chem. Soc.* **2008**, *130*, 17284.
- (25) Ravishankar, R.; Kirschhock, C. E. A.; Knops-Gerrits, P. P.; Feijen, E. J. P.; Grobet, P. J.; Vanoppen, P.; De Schryver, F. C.; Mieke, G.; Fuess, H.; Schoeman, B. J.; Jacobs, P. A.; Martens, J. A. *J. Phys. Chem. B* **1999**, *103*, 4960.
- (26) Kirschhock, C. E. A.; Ravishankar, R.; Verspeurt, F.; Grobet, P. J.; Jacobs, P. A.; Martens, J. A. *J. Phys. Chem. B* **1999**, *103*, 4965.
- (27) Kirschhock, C. E. A.; Ravishankar, R.; Jacobs, P. A.; Martens, J. A. *J. Phys. Chem. B* **1999**, *103*, 11021.
- (28) Kragten, D. D.; Fedeyko, J. M.; Sawant, K. R.; Rimer, J. D.; Vlachos, D. G.; Lobo, R. F. *J. Phys. Chem. B* **2003**, *107*, 10006.
- (29) Ramanan, H.; Kokkoli, E.; Tsapatsis, M. On the TEM and AFM evidence of zeosil nanoslabs present during the synthesis of silicalite-1. *Angew. Chem., Int. Ed.* **2004**, *43*, 4558.
- (30) Kirschhock, C. E. A.; Liang, D.; Aerts, A.; Aerts, C. A.; Kremer, S. P. B.; Jacobs, P. A.; Van Tendeloo, G.; Martens, J. A. *Angew. Chem., Int. Ed.* **2004**, *43*, 4562.
- (31) Lesthaeghe, D.; Vansteenkiste, P.; Verstraelen, T.; Ghysels, A.; Kirschhock, C. E. A.; Martens, J. A.; Van Speybroeck, V.; Waroquier, M. *J. Phys. Chem. C* **2008**, *112*, 9186.
- (32) Aerts, A.; Haouas, M.; Caremans, T. P.; Follens, L. R. A.; van Erp, T. S.; Taulelle, F.; Vermant, J.; Martens, J. A.; Kirschhock, C. E. A. *Chem.—Eur. J.* **2010**, *16*, 2764.

(33) Schoeman, B. J. *Zeolites* **1997**, *18*, 97.

(34) Tsay, C. S.; Chiang, A. S. T. *Microporous Mesoporous Mater.* **1998**, *26*, 89.

(35) Tokay, B.; Somer, M.; Erdem-Senatalar, A.; Schüth, F.; Thompson, R. W. *Microporous Mesoporous Mater.* **2009**, *118*, 143.

(36) Rimer, J. D.; Vlachos, D. G.; Lobo, R. F. *J. Phys. Chem. B* **2005**, *109*, 12762.

(37) Patis, A.; Dracopoulos, V.; Nikolakis, V. *J. Phys. Chem. C* **2007**, *111*, 17478.

(38) Provis, J. L.; Gehman, J. D.; White, C. E.; Vlachos, D. G. *J. Phys. Chem. C* **2008**, *112*, 14769.

(39) de Moor, P. P. E. A.; Beelen, T. P. M.; van Santen, R. A.; Beck, L. W.; Davis, M. E. *J. Phys. Chem. B* **2000**, *104*, 7600.

(40) Rimer, J. D.; Trofymuk, O.; Navrotsky, A.; Lobo, R. F.; Vlachos, D. G. *Chem. Mater.* **2007**, *19*, 4189.

Table 1^a

	TPA ⁺ (mol)	OH ⁻ (mol)	H ₂ O (mol)	M _{SiO₂} (mol L ⁻¹)	M _{OH} (mol L ⁻¹)	pH _{av} , 0 h	pH _{av} , 48 h
starting clear sol	9	9	400	1.76	0.63		
TPAOH13	13	13	467	1.54	0.80	13.3 ± 0.1	13.3 ± 0.5
TPAOH19	19	19	570	1.29	0.98	13.8 ± 0.1	13.8 ± 0.7
CsOH19	9	19	570	1.29	0.98		
TPABr19	19	9	570	1.29	0.63		

^a (Columns 2–4) molar ratios of TPA⁺, OH⁻, and water, for 25 mol TEOS; (columns 5–6) molar concentrations of SiO₂ and OH⁻; (column 7) average pH of sols at the start of dissolution; (column 8) average pH of sols after 48 h of dissolution.

TEOS/TPAOH/H₂O composition of 25:9:400. Dissolution was initiated by increasing the alkalinity of the sol by adding concentrated TPAOH. Because of the high silica concentration, it was possible to monitor the dissolution process by *in situ* static and dynamic light scattering. *In situ* synchrotron SAXS was used to study structural evolution at length scales of the nanoparticles. We performed dissolution experiments on sols at different stages of the crystallization process, starting from the unheated sol of nanoparticles up to the point where relatively large crystals were observed. Our data suggested a peculiar dissolution mechanism, converting entire nanoparticles spontaneously into open clusters of oligomeric silicate species and no gradual decrease of the nanoparticle size. A mathematical model is developed that qualitatively explains the observed dissolution behavior.

Experimental Section

Clear sol was prepared according to the method by Persson et al.⁸ TEOS (tetraethylorthosilicate, Acros, 98%) was added at room temperature to a concentrated aqueous solution of TPAOH (tetrapropylammoniumhydroxide, Alfa Aesar, 40 wt %) under stirring. After hydrolysis of TEOS, bidistilled water was added to the mixture, resulting in a molar TEOS/TPAOH/H₂O ratio of 25:9:400. The mixture was stirred overnight, resulting in the as-prepared clear sol. Before further experiments, the sol was kept at 6 °C.

For SLS/DLS experiments, samples of the as-prepared clear sol were heated at 95 °C in sealed polypropylene bottles for 1, 2, 3, 4, 6, and 8 h for crystallization. The samples were quenched by submerging the hot bottles in cold water and storing at 6 °C. Nanoparticle dissolution was initiated at room temperature by adding amounts of TPAOH 40 wt %, TPABr (98%, Acros), or CsOH (Cesiumhydroxide Monohydrate, 99.5%, Acros) to 5 mL of as-prepared clear sol and each of the 6 heated samples. The molar composition of the samples after the addition of TPAOH, TPABr, or CsOH is given in Table 1. The samples were subsequently stirred for 35 min to ensure homogeneity and then filtered using a 0.2 μm PTFE membrane syringe filter (Alltech) to remove unwanted dust particles that would perturb light scattering experiments.

The addition of extra TPAOH caused a jump of the pH value from 12.5⁹ to above 13 (Table 1). The pH values did not show a clear trend with either heating or dissolution time, i.e., the time after the addition of TPAOH (see Supporting Information, Figure SI-1). pH values averaged over all heating times, with one standard deviation errors, are presented in Table 1.

Filtered samples were loaded into 8 mm diameter glass tubes that were inserted in the sample compartment of an ALV-CGS3 DLS/SLS apparatus equipped with a HeNe laser with a wavelength of 632.8 nm and a power output of 22 mW. *cis*-Decahydronaphthalene (Sigma-Aldrich, 99%) was used as the index matching fluid (*n* = 1.49). For each sample, the static scattered

intensity (SLS) and autocorrelation (DLS) were measured repeatedly at 8 geometrically progressing times between 2 and 170 h after the addition of TPAOH, CsOH, or TPABr, at scattering angles of 45, 60, 90, and 150°. The measurement time per angle was 30–60 s. Relaxation rate distributions were calculated from the autocorrelation functions (ACFs) using the inverse Laplace transformation (ILT) procedure included in the ALV software. ILT analysis with maximum entropy regularization was performed using the Igor Pro software from Wavemetrics. Both analysis methods gave similar results.

For synchrotron SAXS experiments, as-prepared clear sol and clear sol heated at 95 °C for 10, 20, 40, and 70 min, 2 h, and 6 h were combined with 40 wt % concentrated TPAOH solution to provoke dissolution. The final molar TEOS/TPAOH ratio was 25:19. The 7 samples were then stirred at room temperature for 20 min and put into 1 mm glass capillaries (Hilgenberg) that were sealed. The 7 capillaries were mounted on a rack, and SAXS patterns were recorded each 5 min during 5 h at ambient temperature. SAXS patterns were recorded at DUBBLE, the Dutch Belgian Beamline at the European Synchrotron Radiation Facility (ESRF) in Grenoble, France. The accumulation time per sample was 60 s, using a monochromatic X-ray beam (wavelength = 0.1 nm; energy = 12 keV). SAXS patterns were recorded on a two-dimensional (2D) multiwire gas-filled detector with a spatial resolution of 250 μm. The sample-to-detector distance was 1.50 m. The *q*-axis was calibrated using a Ag behenate specimen. Under these conditions, a *q* range between 0.3 and 6.4 nm⁻¹ was covered. The scattering patterns were corrected for detector response, and the intensity was normalized to the intensity of the incoming beam, measured by an ionization chamber placed downstream from the sample. The background of an empty capillary was subtracted from the sample patterns, according to standard procedures, taking into account the sample and sample-holder transmission.

Results

Static (SLS) and dynamic light scattering (DLS) were used to monitor the dissolution of nanoparticles and crystals to silicate oligomers at different stages of the crystallization reaction. For this purpose, a series of seven clear sol samples was prepared, with molar TEOS/TPAOH/H₂O ratio of 25:9:400. A first sample consisted of as-prepared, unheated clear sol. The other samples were obtained by heating the as-prepared clear sol at 95 °C and quenching the reaction after six selected heating times, viz. 1, 2, 3, 4, 6, and 8 h.

Dissolution was performed at room temperature and initiated by adding concentrated 40 wt % aqueous TPAOH solution to small volumes of the unheated and the six heated clear sols. The molar TEOS/TPAOH ratio was decreased from 25:9 to 25:13 (TPAOH13 sample series) and in a second series to 25:19 (TPAOH19 series) (Table 1). Dissolution was

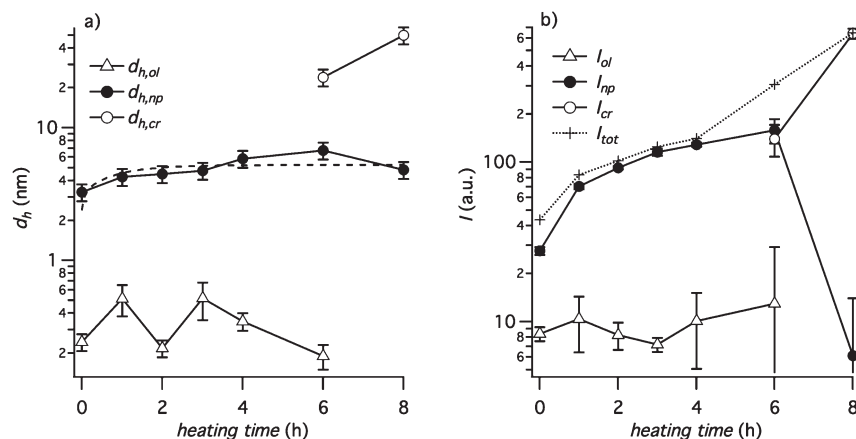


Figure 1. (a) Hydrodynamic diameters d_h of oligomers (ol), nanoparticles (np), and crystals (cr) in sols heated at 95 °C for different times (TPAOH13 series). The data were obtained early (1.9 h) after the start of dissolution at room temperature. The dotted line represents *in situ* measurements conducted at 95 °C.³² (b) Static intensity scattered by each population and total static intensity I_{tot} . Error bars represent the standard deviation of the values at four different scattering angles.

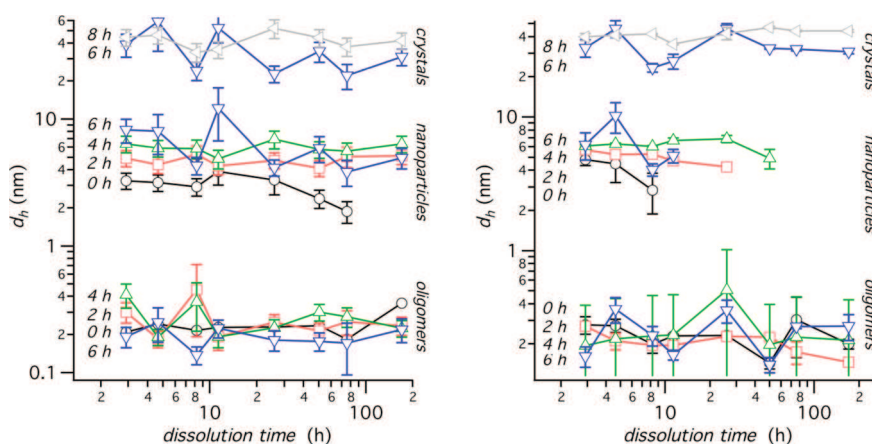


Figure 2. Hydrodynamic diameters d_h of oligomers, nanoparticles, and crystals during dissolution at room temperature. Data for sols heated for 0–8 h at 95 °C before the dissolution experiment are presented. (Left) TPAOH13 series; (right) TPAOH19 series. Each data point is the average value at four scattering angles with error bars representing one standard deviation.

monitored with *in situ*, multiangle, light scattering between ca. 2 and 170 h after the addition of extra TPAOH to the sols.

Light scattering measurements revealed up to three particle populations, depending on heating time and dissolution time. A representative set of light scattering data and their analysis is shown Figure SI-2 of the Supporting Information. For each of the populations, the average hydrodynamic diameter was calculated from the measured diffusion coefficients using the Stokes–Einstein equation. The two particle populations with the smallest diffusion coefficient (largest particle size) were assigned to nanoparticles and crystals.^{9,10} The third DLS signal, having the largest diffusion coefficient, was attributed previously to a second diffusive motion of nanoparticles termed collective diffusion.^{9,10} Collective diffusion occurs in concentrated systems and involves the correlated motion of many particles, as opposed to the self-diffusive motion of individual particles.⁴¹ However, in the present work, the fast diffusing population was still observed when nanoparticles had completely dissolved

into silicate oligomers (see Figures 2 and 3 below). This strongly suggested that the fast DLS signal was caused by the diffusion of oligomers instead of the collective diffusion of nanoparticles.

Crystallization Monitored with Light Scattering. Sols at different stages of the crystallization, i.e., after different heating times, were characterized by light scattering. These measurements were conducted early in the dissolution process (1.9 h after the addition of extra aqueous TPAOH) to evaluate the initial state of the sols before significant dissolution had occurred.

Until 4 h of heating, only oligomers and nanoparticles were observed (Figure 1). Note that oligomers were already observed in this early stage of the dissolution process. This was expected because a clear sol of the present composition contains a small amount of oligomers even before the addition of extra TPAOH.^{9,10} Oligomers in the clear sol typically consist of 1 to 10 Si atoms.⁴²

With increasing heating time, the average oligomer size fluctuated between 0.2 and 0.6 nm. It was not possible to

(41) Pusey, P. N.; Fijnaut, H. M.; Vrij, A. *J. Chem. Phys.* **1982**, *77*, 4270.

(42) Haouas, M.; Petry, D. P.; Anderson, M. W.; Taulelle, F. J. *Phys. Chem. C* **2009**, *113*, 10838.

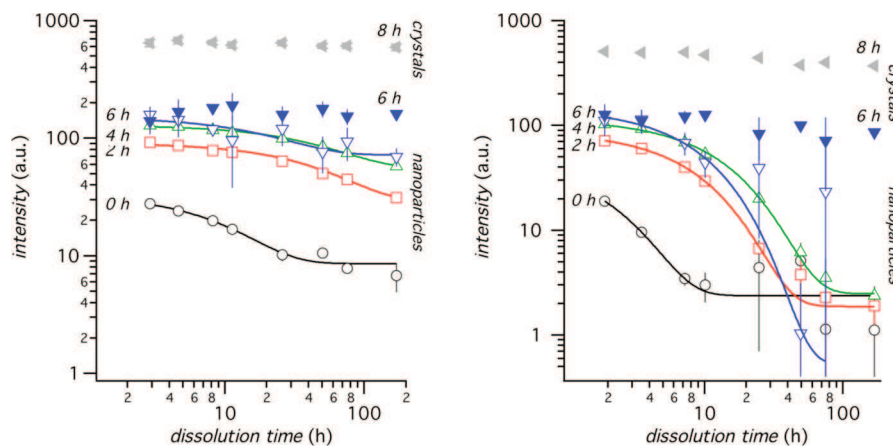


Figure 3. Evolution of static intensity of nanoparticles and crystals during dissolution at room temperature. Data for sols heated for 0–8 h at 95 °C before the dissolution experiment are presented. The solid traces are exponential fits to the data. (Left) TPAOH13 series; (right) TPAOH19 series. Each data point is the average value at four scattering angles with error bars representing one standard deviation.

identify a trend of the oligomer size within experimental error. But the order of magnitude of the oligomer size was realistic, given that the length of a Si–O–Si bond is 0.3 nm.

The size of nanoparticles increased from 3 to 5 nm, in agreement with previously reported DLS data measured at crystallization temperature (95 °C, dotted line in Figure 1a).³² After 6 h, the first crystals were resolved. The diameter of the first crystals was ca. 30 nm, growing to ca. 50 nm after 8 h.

The total static intensity I_{tot} and that of the three populations separately are shown in Figure 1b. The intensity of the oligomers was small and constant within experimental error. The intensity of nanoparticles I_{np} increased with heating time, consistent with the increase of their size. On the basis of the sudden increase of the total static intensity, the onset of crystal growth occurred between 4 and 6 h of heating (Figure 1b). After 8 h, the intensity of oligomers and nanoparticles became very small relative to that of the crystals. The oligomers could not be observed any more, but the nanoparticle population was still detectable, and its size was in agreement with the previously reported DLS data at 95 °C. However, the intensity scattered by nanoparticles in the 8 h was underestimated in the DLS analysis. A large fraction of the nanoparticle intensity was counted as a part of the crystal intensity. This was further evident from the evolution of static intensity during the dissolution described below.

For the more alkaline TPAOH19 series, similar trends of the particle size and intensity with heating time were observed (Supporting Information, Figures SI-3 and SI-4). The hydrodynamic particle sizes differed slightly in magnitude from those of the TPAOH13 series, but the intensities, after correction for the silicon concentration in the sols, superimposed.

On the basis of these results, the period between 0–4 h of heating was taken as the induction stage of crystallization and is characterized by the growth of nanoparticles. Nucleation and growth of crystals started between 4 and 6 h. Under the present synthesis conditions, the

crystals grew further, reaching a final diameter of 100 nm after 20 h.³² Thus, the investigated 8 h heating period covered the induction stage, nucleation, and the onset of crystal growth.

Dissolution Monitored with Light Scattering. Between 2 and 170 h after the addition of extra TPAOH to the samples, the hydrodynamic diameter of the three populations remained almost constant (Figure 2). The static intensity scattered by nanoparticles decreased strongly (Figure 3), whereas the intensity of oligomers (Supporting Information, Figure SI-5) and crystals (Figure 3) remained at the same level. The constant nanoparticle diameter was a surprising result and was most clearly observed for the sols heated between 1 and 4 h (see Figure SI-6 of the Supporting Information for samples heated for 1 and 3 h). Among the different heating times, the 1–4 h data are probably the most accurate because the share of nanoparticles in the total intensity is highest (Figure 3).

The combined trends of size and intensity suggested that nanoparticles dissolved by rapid disintegration of entire particles. At constant nanoparticle diameter d , the principal cause for the strong decrease of the nanoparticle intensity is a decrease of the number of nanoparticles N because the intensity is proportional to Nd^6 .

Crystals dissolved at a much slower rate than nanoparticles, revealed by their almost constant hydrodynamic diameter and intensity (Figures 2 and 3). The crystals intensity of the 8 h heated sols showed a small decrease, but this could be accounted for by the intensity loss caused by the dissolution of nanoparticles that were not resolved from the crystal signal in DLS.

The constant diameter of oligomers suggested that oligomers of similar size were formed during the entire dissolution process. The continuous formation of new oligomers out of dissolving nanoparticles should result in an increase of the corresponding static intensity. However, a significant increase was not observed (Supporting Information, Figure SI-5), probably because the oligomer intensity was too small compared to the background. Oligomers were still observed after complete nanoparticle dissolution. This observation confirmed the assumption

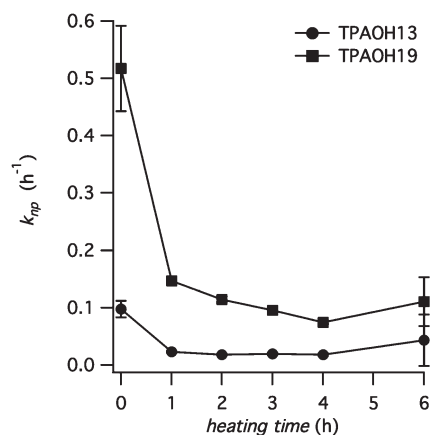


Figure 4. Rate constants (k_{np}) of the exponential decay of intensity scattered by nanoparticles during their dissolution at room temperature, for sols heated at 95 °C for different times. Data for two TPAOH concentrations are shown (TPAOH13 and TPAOH19 series). The error bars represent one standard deviation of the fitted rate constants.

that this DLS signal specifically relates to the diffusion of oligomers.

To quantify the influence of different heating times on nanoparticle dissolution rates, the decrease of nanoparticle intensity with dissolution time, $I_{np}(t)$, was fitted, error weighted with an exponential decay to a baseline intensity I_b (Figure 3):

$$I_{np}(t) = I_{np}(0)\exp(-k_{np}t) + I_b \quad (1)$$

The dissolution rate constants k_{np} decreased monotonously with heating time up to 4 h (Figure 4). The decrease of rate constants was largest between 0 and 1 h of heating. At 6 h, a slight increase was observed, probably arising from the difficult simultaneous analysis of nanoparticles and crystals, evident from the large error of the 6 h data points. The rate constants of the more alkaline TPAOH19 dissolution series were consistently 5 times larger than those of the TPAOH13.

A control experiment in which aqueous TPABr was added to the sols instead of TPAOH (Table 1) did not result in an evolution of the static scattering intensity. This experiment showed that the changes observed when adding aqueous TPAOH are predominantly caused by the increase of hydroxyl anion concentration rather than by the increase of $[TPA^+]$ or dilution effects. In another series of experiments, CsOH was added to initiate dissolution (Table 1). The addition of CsOH and TPAOH at the same molar concentration had a similar dissolution effect (data for CsOH not shown). The nature of the cation (Cs^+ versus TPA^+) had little influence on nanoparticle dissolution kinetics, confirming that the hydroxyl anion concentration was the relevant parameter.

Dissolution Monitored with SAXS. The dissolution of nanoparticles into oligomers after adding TPAOH was also monitored with *in situ* SAXS (for the TPAOH19 composition; Table 1). SAXS patterns were recorded approximately every 15 min over the first 5.5 h of the dissolution process, and a final pattern was recorded after 18–19 h. Dissolution experiments were carried out on

sols quenched during the induction period of the crystallization, viz., after heating times between 0 and 120 min. In this period, the nanoparticles showed the largest evolution of their size (Figure 1) and dissolution rate (Figure 4). Representative SAXS dissolution data of sols heated for 10 and 120 min are shown in Figure 5. Patterns for four other heating times are provided in Supporting Information (Figure SI-7).

The patterns showed two features. The intensity decay below $q \sim 2.5 \text{ nm}^{-1}$ was associated with the form factor of individual nanoparticles. The peak at $q \sim 3.2 \text{ nm}^{-1}$ was ascribed to oligomers. The clear peak suggested that the oligomers were strongly correlated in the sols. During dissolution, the intensity of the low- q nanoparticle feature decreased, whereas the oligomer scattering at $q \sim 3.2 \text{ nm}^{-1}$ gained intensity. After 18–19 h, light scattering showed that the dissolution of nanoparticles to oligomers was complete (Figure 3b). Correspondingly, in the SAXS patterns after 18–19 h, the oligomer peak was the dominant feature.

The average spacing between oligomers could be estimated from the position of the peak maximum, being $2\pi/q = 1.9 \text{ nm}$. Surprisingly, the position of the oligomer peak was independent of dissolution time, thus revealing a constant distance between oligomers.

Another remarkable feature was the presence of an iso-scattering point where all of the SAXS patterns crossed (Figure 5). The intensity and position of the iso-scattering point were invariant during the entire dissolution process. The iso-scattering point indicated that only two types of structures were involved during dissolution, which changed in relative population, but not in size, shape, or structure. Consistent with the analysis of diffusion coefficients and static intensity (Figures 2 and 3), the iso-scattering points hence indicated that nanoparticles disintegrated directly to oligomers. This process leads to a decrease of the nanoparticle number but not of their size.

On this account, the SAXS patterns $X(t)$ at different dissolution times t were simulated with a weighted sum of the pattern of 100% nanoparticles X_{np} and that of 100% oligomers X_{ol} :

$$a(t)X_{np} + [1 - a(t)]X_{ol} = X(t) \quad (2)$$

Details on the calculation and examples of simulations are provided in Supporting Information. Briefly, the 100% nanoparticle pattern was first calculated, assuming power law decay at large q . The weighing factors $a(t)$ were determined by minimizing the sum of squared differences between experimental and calculated composite patterns.

The weighing factors $a(t)$ and $1 - a(t)$ in eq 2 are proportional to the number of nanoparticles and oligomers, respectively, although the proportionality constants are unknown and are for certain different for both species. The evolution of the weighing factors $a(t)$ with dissolution time is shown in Figure 6a. Analogous to the analysis of light scattering intensity, the weighing factors were fitted with a single exponential decay (Figure 6a). The exponential function described the data remarkably well. The decay rate constants from fits to $a(t)$ (Figure 6b)

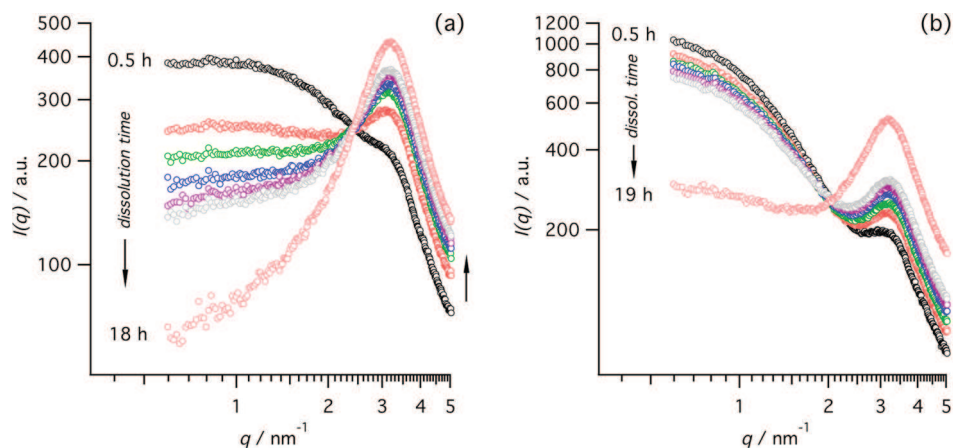


Figure 5. SAXS patterns recorded during dissolution at room temperature of clear sol (TPAOH19 series) heated at 95 °C for 10 min (a) and for 2 h (b).

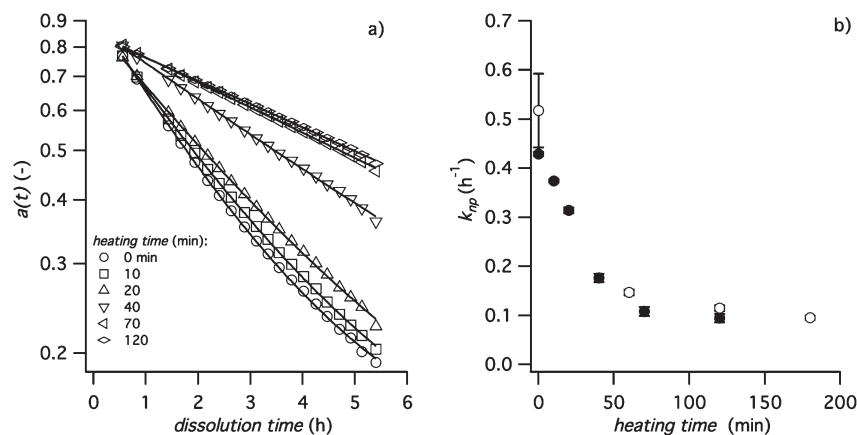


Figure 6. (a) Evolution of weighing factors $a(t)$ with dissolution time at room temperature (TPAOH19 series) for different heating times at 95 °C. The solid black lines are single exponential fits to the data. (b) Exponential dissolution rate constants k_{np} of nanoparticles derived from SAXS (■) and DLS/SLS (○). The error bars represent one standard deviation of the fitted rate constants.

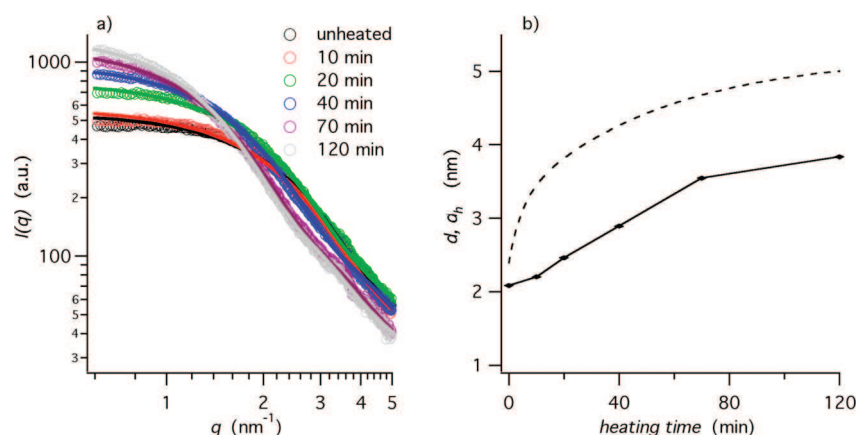


Figure 7. (a) Calculated SAXS patterns of 100% nanoparticles for different heating times at 95 °C. The solid lines are fits with an oblate ellipsoid form factor; (b) major ellipsoidal axis (d) derived from SAXS fitting. The dotted line is the hydrodynamic diameter (d_h) of nanoparticles determined with *in situ* DLS at 95 °C.³²

decreased with heating time and were in good agreement with the corresponding rates determined from light scattering.

From the simulations, the 100% nanoparticle patterns X_{np} at different heating times could be calculated (Figure 7a). At all heating times, the patterns exhibited power law exponents of ca. -2 at high q -values, in agreement with open, mass fractal aggregate, or disk- or sheet-like structures. To estimate

the size of the nanoparticles, the patterns were fitted with an oblate ellipsoidal form factor. This shape was used previously to describe the scattering of nanoparticles in dilute sols.⁴⁴ The ellipsoidal model described the data with reasonable accuracy

(43) Fedeyko, J. M.; Vlachos, D. G.; Lobo, R. F. *Langmuir* **2005**, *21*, 5197.

(44) Groen, J. C.; Hamminga, G. M.; Moulijn, J. A.; Perez-Ramirez, J. *Phys. Chem. Chem. Phys.* **2007**, *9*, 4822.

(Figure 7). In the present case, only the length of the major ellipsoidal axis could be determined from the fits because the -2 power law decay extended to the end of the measured q range, i.e., there was no transition to surface scattering at length scales of the minor ellipsoidal diameter. Irrespective of the exact shape and structure of the nanoparticles, however, the fitted ellipsoidal diameter provided an estimate of the largest dimension of the nanoparticles.

The diameter of nanoparticles derived from SAXS analysis increased with heating time, following a trend similar to that of the hydrodynamic diameters determined by DLS (Figure 7b). There was a difference of about 1 nm between SAXS and DLS diameters, which could be attributed to the core-shell structure of the nanoparticles.⁴³ Because of its high scattering contrast, only the nanoparticle silica-rich core is measured with SAXS, whereas DLS measures the hydrodynamic size which includes a shell of adsorbed TPA and solvent molecules. On the basis of the present results, the thickness of the shell was about 0.5 nm.

Discussion

Nanoparticles in clear sol dissolved into smaller silicate oligomers when the alkalinity was increased by the addition of aqueous TPAOH. Light scattering and SAXS consistently revealed that the number rather than the size of the nanoparticles decreased during dissolution. The single exponential decay of the intensity suggested that the dissolution rate was first order in the nanoparticle number density (number of nanoparticles per unit volume sol).

The dissolution rate constants of the nanoparticles decreased with heating time of the sol (Figures 4 and 6b). This decrease was attributed previously to the increasingly zeolite-like silicate structure of the nanoparticles during the induction stage.⁴⁰ The present results revealed a clear trend between dissolution rate constants k_{np} and the particle size, i.e., the size of the nanoparticle's silica core as estimated by SAXS (Figure 7b). This observation suggested that particle size effects, besides structural changes of the silicate framework, contributed to the decrease of the nanoparticle dissolution rate. In particular, the relationship between nanoparticle size and dissolution rate constants could be described with a power law with an exponent close to -3 , suggesting that the rate constants were inversely proportional to the nanoparticle core volume (Figure 8). This observation will be taken into account in a mathematical dissolution model that is outlined below.

The decrease of nanoparticle number rather than size was unexpected. Large colloidal silica particles, such as 100 nm amorphous silica and 65 nm Silicalite-1, dissolve through gradual, linear decrease of the particle radius with dissolution time, at constant particle number density.⁴⁰ In these cases, dissolution was described by stepwise detachment of silicate monomers from the silica particle. However, at elevated pH and silica concentration, dissolution proceeds by detachment of silicate oligomers rather than monomers. This was observed for amorphous silica and quartz, and

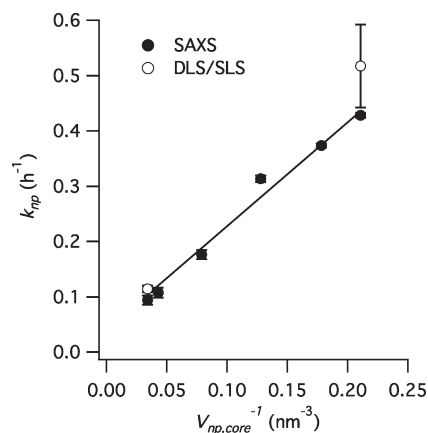


Figure 8. Dissolution rate constants determined with SAXS and light scattering versus reciprocal nanoparticle core volume. The solid line is a linear fit to the data. One standard deviation error bar of the rate constants was determined from exponential fitting of the intensity decay curves.

more recently for MFI-type zeolite crystals using *in situ* ATR-IR spectroscopy.⁴⁴

The dissolution of Silicalite-1 precursor nanoparticles of ca. 3–4.5 nm diameter was studied by Rimer et al.⁴⁰ Initially, the dissolution of these nanoparticles was similar to that of much larger silica particles, i.e., through linear decrease of the particle size with dissolution time at constant particle number density. However, after longer dissolution times, the authors observed the fragmentation of nanoparticles.⁴⁰ These fragments were described as small nanoparticles rather than as large oligomers. In the present study, dissolution was carried out at comparably high silica concentration and alkalinity. Therefore, it is likely that dissolution proceeded through the detachment of silicate oligomers rather than monomers.

The silicate oligomers gave rise to a correlation peak in the SAXS patterns, which increased in intensity but remained at the same position while dissolution proceeded (Figure 5). If the oligomers formed upon dissolution would be distributed uniformly in the sol, a shift of the correlation peak to larger q would be expected because the increase of the number density of oligomers would cause a reduction of the average distance between them. The constant position of the SAXS oligomer peak hence suggested that the oligomers were not uniformly distributed in solution but were confined in a separate phase that expanded upon dissolution and in which their number density was constant. However, actual phase separation was not observed at macroscopic length scales, nor at length scales monitored by light scattering ($2\pi/q = 600$ – 1900 nm). The constant interoligomer spacing and the absence of large-scale phase separation are rationalized by accepting the fact that after dissolution of a nanoparticle, the resulting oligomer fragments form a stable cluster in which the average separation between individual oligomers is constant, approximately $2\pi/3.2 = 1.9$ nm from the position of the peak. The size of the cluster can be estimated from the nanoparticle diameter before dissolution. A nanoparticle core diameter of 3.5 nm

(after 1 h of heating; Figure 7b) corresponds to ~ 10 Si–O–Si bonds, each measuring ~ 0.3 nm. Assuming that the nanoparticle is transformed to a cluster with oligomer fragments that typically contain 2 silicon atoms in one dimension (e.g., a cubic octamer oligomer), the cluster will contain approximately 5 fragments along its diameter, giving a diameter of roughly 10 nm. The open clusters may be stabilized by the incorporation of TPA^+ captions between oligomer fragments. TPA^+ is known for its affinity for small silicate oligomers.⁴⁵ The formation of physically bound clusters of oligomers is consistent with the recent work by Petry et al. who observed that nanoparticles are formed by physical aggregation of oligomers with partial siloxane bond formation between the aggregated oligomers.⁴⁶ The scattering of entire oligomer clusters is not observed with SAXS or light scattering, probably due to their low contrast with the surrounding sol at length scales of the cluster size. After all, the solvent surrounding the clusters (or nanoparticles) contains a low concentration of isolated oligomers ($\sim 10\%$ of the total Si atom content), even before dissolution.^{9,10}

Mathematical Model for Nanoparticle Dissolution. We here propose a phenomenological model based on the following experimental observations: (i) nanoparticles seem to decompose in one step into oligomers, i.e., no intermediate particles are found (nanoparticles with one or more detached oligomers). (ii) The rate of the effect scales is inversely proportional with the nanoparticle volume (Figure 8). Observation i indicates that the dissolution of the particle is initiated by a sudden event, the rate-determining step, after which the particle quickly falls apart. The most straightforward mechanism for such an initiating event would be the extraction of one molecular oligomer cluster from the surface of the nanoparticle after which the whole nanoparticle destabilizes and decomposes into a cluster of oligomers. However, one would expect that the rate (the probability of extraction) of such a process scales with the surface r^2 of the nanoparticle, r being the radius of the nanoparticle, instead of the observed r^{-3} (Figure 8).

We will show that the observed experimental behavior can be modeled by a discrete random motion along a one-dimensional (1D) reaction coordinate which we take to be the number of extracted oligomers from the nanoparticle. From the experimental observations, we can show that the corresponding free energy barrier, which is a function of the reaction coordinate, is sharply increasing at the start and then continues to increase with a positive, though declining, slope. This shows that the extraction of the first oligomer from the nanoparticle is the most difficult, but the extraction of the following oligomers becomes more and more easy along the way. However, as long as the partly dissolved nanoparticle is still of appreciable size, it is likely that it will regrow to its original size rather than dissolve completely.

For a barrier, consisting of a 1D sequence of metastable states, exact expressions for the reaction rate can be derived.⁴⁷ In this view, M_0 and M_n label the stable states A (initial nanoparticle) and B (final oligomer cluster). The rate k_{AB} thus equals the experimental rate k_{np} shown in Figure 8. However, to go from state M_0 to M_n , the system has to surpass $n - 1$ metastable states (partially dissolved nanoparticles; n equals the number of detached oligomers) in between, M_1, M_2, \dots, M_{n-1} . These states are considered to be higher in free energy and, therefore, relatively low in population. Transitions will only occur between neighboring states after which we assume the system will always equilibrate before a new transition takes place. The transition from A to B is then determined by discrete Markovian hopping dynamics determined by the hopping probabilities.

The overall rate $k_{AB} = k_{0,n}$ obeys the following recursion relationship:

$$k_{0,n} = k_{0,1} T[1 \rightarrow n] \\ T[1 \rightarrow j+1] = \frac{\tau_{j,j+1} T[1 \rightarrow j] T[1 \rightarrow j-1]}{T[1 \rightarrow j-1] - (1 - \tau_{j,j+1}) T[1 \rightarrow j]} \quad (3)$$

Equation 3 is equivalent to eq 2 in ref 47 (see Supporting Information) but is more convenient to derive the forthcoming expression for the free energy barrier.

Here, $k_{0,1}$ is the initial rate of $M_0 \rightarrow M_1$, which is assumed to be the rate determining step. $\tau_{j,j+1}$ is the one-step hopping probability to transfer from metastate j to $j + 1$ rather than to $j - 1$. Conversely, $\tau_{j,j-1} = 1 - \tau_{j,j+1}$ is the chance that the system moves backward instead of forward. $T[1 \rightarrow j]$ is the probability that a sequence of hopping transitions starting from M_1 will first visit M_j before M_0 . The transition probability $\tau_{j,j+1}$ on the barrier is related to the rates $k_{j,j\pm 1}$ via

$$\tau_{j,j+1} = \frac{k_{j,j+1}}{k_{j,j+1} + k_{j,j-1}} \quad (4)$$

Hence, the absolute rates $k_{j,j\pm 1}$ (as long $\gg k_{0,1}$) have no influence on the overall rate; only the relative value is important.

Once all transitions probabilities $\tau_{j,j+1}$ and the initial rate $k_{0,1}$ are known, eqs 3 allow one to calculate the overall rate $k_{AB} = k_{0,n}$, in an iterative manner. Starting from $T[1 \rightarrow 1] = 1$ and $T[1 \rightarrow 2] = \tau_{1,2}$, we can successively solve eq 3 for $j = 2, 3, \dots, n$.

We can distinguish the following characteristic type of dynamics.

- $\tau_{j,j+1} \gg \tau_{j,j-1}$ for all j : the overall rate $k_{0,n} \approx k_{0,1}$ is independent of n (for the moment, we are treating $k_{0,1}$ as a constant, but we will come back to this point when discussing the dissolution dynamics).
- $\tau_{j,j+1} = a \ll \tau_{j,j-1}$ for all j : the overall rate will show an exponential dependence on n : $k_{0,n} \approx k_{0,1} a^n$.
- $\tau_{j,j+1} = \tau_{j,j-1} = 1/2$ for all j : the overall rate becomes inversely proportional with n ⁴⁷: $k_{0,n} \approx k_{0,1}/n$.

(45) Pelster, S. A.; Schröder, W.; Schüth, F. *J. Am. Chem. Soc.* **2006**, *128*, 4310.

(46) Petry, D. P.; Haouas, M.; Wong, S. C. C.; Aerts, A.; Kirschhock, C. E. A.; Martens, J. A.; Gaskell, S. J.; Anderson, M. W.; Taulelle, F. *J. Phys. Chem. C* **2009**, *113*, 20827.

(47) Moroni, D.; Bolhuis, P. G.; van Erp, T. S. *J. Chem. Phys.* **2004**, *120*, 4055.

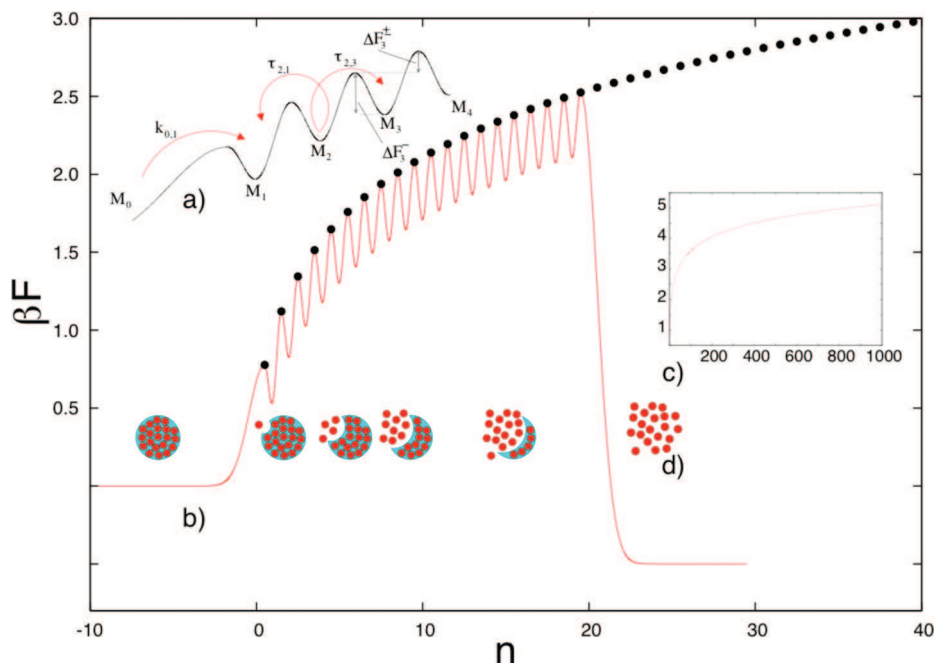


Figure 9. Free energy barrier profile derived from the theoretical model with $\mu = 5/3$. Panel a shows the definitions of $k_{0,1}$, $\tau_{2,1}$, $\tau_{2,3}$, ΔF_3^- , and ΔF_3^+ . (Panel b) The free energy profile for a particle consisting of $n = 20$ silicate oligomer units. Depth of the wells and initial and final free energy plateaus are chosen arbitrarily, as they do not follow from the model. Only the free energy differences between the maxima of the intermediate barriers (black dots) are given by the model. Panel c shows the same free energy profile at a larger scale (up to $n = 1000$). (Panel d) Pictorial sketch of the nanoparticle's dissolution process.

In relation to the dissolution experiment, M_j would refer to a state in which j silicate oligomers (units) have been extracted from a nanoparticle. When the initial nanoparticle consists of n units, the reactant and product states are denoted by M_0 and M_n , respectively. $k_{0,1}$ is the rate to extract the first cluster from the nanoparticle. We will assume that every silicate unit at the surface has an equal chance to be dissolved and that the rate of dissolution is independent of heating time, which implies that it is independent of the size of the nanoparticle and of the nanoparticle framework structure. However, the dissolution rate of *any* silicate unit, $k_{0,1}$, scales with the surface of the nanoparticle or $k_{0,1} \propto r^2 \propto n^{2/3}$. Naturally, this requires that $T[1 \rightarrow 0] \propto n^{-5/3}$ to explain the scaling $k_{AB} = k_{np} \approx 1/n$ that was found experimentally (Figure 8).

Although we should bear in mind that the experimental scaling law is only valid up to some very crude approximations, in the following we will assume that $T[1 \rightarrow 0]$ is exactly proportional to $j^{-\mu}$. For $\mu = 1$, we obtain dynamics c. When $\mu > 1$ the dynamics are in between that of b and c. Bringing $\tau_{j,j+1}$ in front of eq 3 and substituting $T[1 \rightarrow 0] = j^{-\mu}$ yields

$$\tau_{j,j+1} = \frac{j^\mu - (j-1)^\mu}{(j+1)^\mu - (j-1)^\mu} \quad (5)$$

From this, we can get partial information about the free energy barrier as follows:

$$\begin{aligned} \tau_{j+1} &= \frac{k_{j,j+1}}{k_{j,j-1} + k_{j,j+1}} = \frac{Ae^{-\beta\Delta F_j^+}}{Ae^{-\beta\Delta F_j^-} + Ae^{-\beta\Delta F_j^+}} \\ &= \frac{e^{-\beta\Delta F_j^+}}{1 + e^{-\beta\Delta F_j^-}} \end{aligned} \quad (6)$$

with A being the pre-exponential constant and $\Delta F_j^\pm = \Delta F_j^+ - \Delta F_j^-$ which is the free energy difference between

the left and right transition barrier viewed from M_j (see Figure 9).

Inverting eq 6 and substituting eq 5 gives

$$\beta\Delta F_j^\pm = \ln\left(\frac{1 - \tau_{j,j+1}}{\tau_{j,j+1}}\right) = \ln\left(\frac{(j+1)^\mu - j^\mu}{j^\mu - (j-1)^\mu}\right) \quad (7)$$

The overall free energy profile is then obtained by $\beta F_n = \sum_{j=1}^n \Delta F_j^\pm$, which is depicted in Figure 9. In the limit $j \rightarrow \infty$ we can expand eq 7 in terms of $1/j$ which results in $\beta\Delta F_j^\pm = (\mu - 1)/j$. This implies that such a barrier is indeed flattening but that the overall barrier does not have a final maximum plateau as $\sum_{j=1}^n 1/j = \infty$ if $n \rightarrow \infty$.

Although eq 7 has been derived on the basis of a single experimental approximate scaling law, the model offers explanations for several other experimental observations. The rapid initial increment of the free energy barrier accounts for the absence of intermediately sized particles in the dissolution process. Moreover, the experimental evidence that the nanoparticle's oligomer fragments do not spread but remain confined within a cluster corroborates with diffusive dynamics along the reaction coordinate; as the extracted silicate cluster remains close to the dissolving nanoparticle, it can easily reattach again. In conclusion, although eq 7 is based on crude approximations, it elegantly explains the experimental findings. We therefore believe that the idealized model as depicted in Figure 9 might actually give a good qualitative picture of the actual mechanism.

In the model, the decrease of nanoparticle dissolution rate with heating time is a consequence of particle size only. Changes of the silicate framework are not accounted for. Thus, the model is consistent with crystallization models in

which the increase of the nanoparticle size is the dominant phenomenon during the induction stage (until 4 h in the present work). In the nanoslab model,^{25–27} nanoparticles are uniformly zeolite structured and maintain this structure during induction while their size increases. Dissolution rates of such uniformly structured particles are expected to be dependent on particle size only. However, Davis et al. suggested that during the induction stage only a minor fraction of nanoparticles obtains zeolite-like structure.²² The majority of nanoparticles do not undergo structural changes. Structural changes of a small fraction of nanoparticles should not affect the overall dissolution rate. Therefore, also in the model by Davis et al., dissolution rates should be predominantly determined by particle size.

Conclusions

Insight into the chemistry of precursor nanoparticles in concentrated clear sols at different stages of Silicalite-1 zeolite synthesis was gained through *in situ* static and dynamic light scattering and small-angle X-ray scattering. The dissolution process of nanoparticles upon the addition of TPAOH solution could be investigated using these techniques. Light scattering experiments showed that nanoparticles retain their original size until they are decomposed rapidly into a cluster of oligomers. Consistent with these observations, SAXS patterns during dissolution could be modeled assuming a decreasing number of nanoparticles of constant size and an increasing number of oligomers. Nanoparticle decomposition rates could be determined from the decay of light scattering intensity and SAXS modeling. Among the nanoparticles, the largest ones occurring in the course of crystallization disintegrated most slowly. The disintegration rate constant scaled inversely proportional to the nanoparticle volume.

The experimentally observed disintegration behavior was modeled by assuming that a nanoparticle dissolved to oligomers via a series of partially dissolved nanoparticles that correspond to metastable intermediate states of increasing free energy. A dissolving nanoparticle has to

overcome the free energy barrier imposed by partially dissolved states before complete conversion to oligomers. Using the experimental input, the free energy barrier could be derived and was found to have a positive, though declining, slope. The idealized free energy profile provided a qualitative explanation for the apparent instantaneous disintegration of entire nanoparticles. The model supports the assumption that an increase of the nanoparticle size contributes to its stability during the induction stage of zeolite crystallization. This size-based stabilization adds to the earlier observed evolution of the internal connectivity toward a more zeolite-like structure. The results of this work are useful to understand and predict the response of nanoparticles to the upswing of the sol pH occurring spontaneously near the end of zeolite crystallization.

Acknowledgment. We acknowledge the European Synchrotron Radiation Facility for provision of synchrotron radiation facilities, and we thank Nicolas Vilayphiou for assistance in using beamline BM26 DUBBLE. We are grateful to M. Haouas and F. Taulelle for the many helpful and stimulating discussions. We thank F.W.O.-Vlaanderen for supporting the DUBBLE project. T.P.C. acknowledges the Institute for the Promotion of Innovation through Science and Technology in Flanders (IWT-Vlaanderen), for a Ph.D. scholarship. C.E.A.K., J.A.M., and L.R.A.F. acknowledge financial support by ESA and the Belgian Prodex office. A.A. is grateful to the Flemish FWO for a postdoctoral scholarship. This work was supported by the Belgian government through the IAP–PAI network and by the Flemish government through long term structural funding to J.A.M. (Methusalem).

Note Added after ASAP Publication. There was a minor text error in the Results and Discussion section in the version published ASAP May 14, 2010; the corrected version was published ASAP May 18, 2010.

Supporting Information Available: pH measurements, light scattering data, simulations of SAXS patterns, and mathematical derivations (PDF). This material is available free of charge via the Internet at <http://pubs.acs.org>.

Supporting Information

1. Sol pH during heating and dissolution

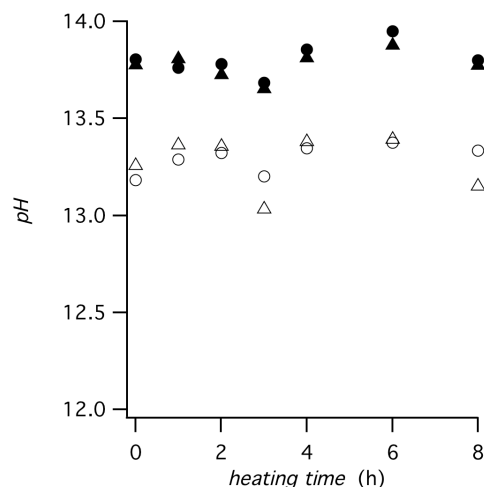


Figure SI-1. pH (open symbols) TPAOH13 series; (filled symbols) TPAOH19 series immediately after addition of extra TPAOH (circles) and after two days (triangles).

2. Light scattering

2.1 Representative light scattering data and analysis

A representative set of light scattering data and their analysis is shown Figure SI-2. These data were obtained from the 6 h sample of the TPAOH13 series, 8 h after the start of dissolution. Figure SI-2a shows the autocorrelation functions $g_1(t)$ at four scattering angles θ , where t is the lag time. In general, the autocorrelation function is the sum of exponential relaxation modes i each having a characteristic relaxation time τ_i and amplitude A_i .^[8]

$$g_1(t) = \sum_i A_i(\tau_i) \exp(-t/\tau_i) \quad \text{Eq. SI-1}$$

Relaxation time distributions $A_i(\tau_i)$ showed one, two or three modes, depending on heating and dissolution time. The example of Figure SI-2 presents a three-mode case (Figure SI-2b).

Previous work showed that the slower two modes are caused by diffusion nanoparticles (*np*) and crystals (*cr*).^[9,10] The fast decaying mode, labeled “oligomers” (*ol*) in Figure SI-2b, is attributed to oligomers in this work.

For each mode, the peak position (at maximum amplitude) and area were determined by fitting the peaks with Gaussian distributions (not shown). Peak position and area were used as estimates for τ_i and A_i , respectively. The relaxation times τ_i of the three modes depended on the scattering vector q according to

$$\frac{1}{\tau_i} = D_i q^2 \quad \text{Eq. SI-2}$$

where D_i is the diffusion coefficient (Figure SI-2c).^[8] This relation confirmed that the modes stemmed from diffusive processes. Diffusion coefficients reported in this work were determined from error weighted linear fits according to Eq. SI-2. For the sample shown in Figure SI-2, the diffusion coefficients were $D_{ol} = 37 \pm 5 \times 10^{-11}$, $D_{np} = 1393 \pm 5 \times 10^{-14}$, $D_{cr} = 2320 \pm 8 \times 10^{-15} \text{ m}^2\text{s}^{-1}$. The errors represent the standard deviation of the fitted diffusion coefficients. Note that the relative error of the oligomer diffusion coefficient is much larger, due to the low scattering intensity associated with this population. These diffusion coefficients were further used to calculate hydrodynamic particle sizes. Application of the Stokes-Einstein equation, with a sol viscosity of $6.63 \pm 0.96 \text{ mPa s}$, yielded hydrodynamic diameters of $0.18 \pm 0.03 \text{ nm}$, $4.7 \pm 0.7 \text{ nm}$, $28.6 \pm 4.2 \text{ nm}$ for oligomers, nanoparticles and crystals, respectively. The errors on the diameters were calculated using the appropriate error propagation formulas.

With these three diffusive modes, the correlation function can be written as:

$$g_1(t, q) = A_{ol} \exp(-D_{ol} q^2 t) + A_{np} \exp(-D_{np} q^2 t) + A_{cr} \exp(-D_{cr} q^2 t) \quad \text{Eq. SI-3}$$

with

$$A_{ol} + A_{np} + A_{cr} = 1$$

because of normalization to $g_1(0, q)$. The amplitudes A_i ($i=ol, np, cr$) represent the fraction of the total static intensity I scattered by oligomers, nanoparticles and crystals respectively:

$$\begin{aligned}
 I_{ol} &= A_{ol}I \\
 I_{np} &= A_{np}I \\
 I_{cr} &= A_{cr}I
 \end{aligned}$$

Eq. SI-4

The total static intensity I was independent of q , or, equivalently, the scattering angle (Figure SI-2d). The individual components of the intensity showed slight q -dependence (Figure SI-2d), probably arising from the inaccuracy of determination of the amplitudes in the ILT fit. In this work, intensities averaged over the four scattering angles are reported, with an error representing one standard deviation.

In conclusion, light scattering experiments yielded the diffusion coefficients for each population, which could be used to calculate hydrodynamic particle sizes d_h . The static intensities provided information on the (static) particle size and number density N , because $I \sim NV^2$, where V is the particle volume.

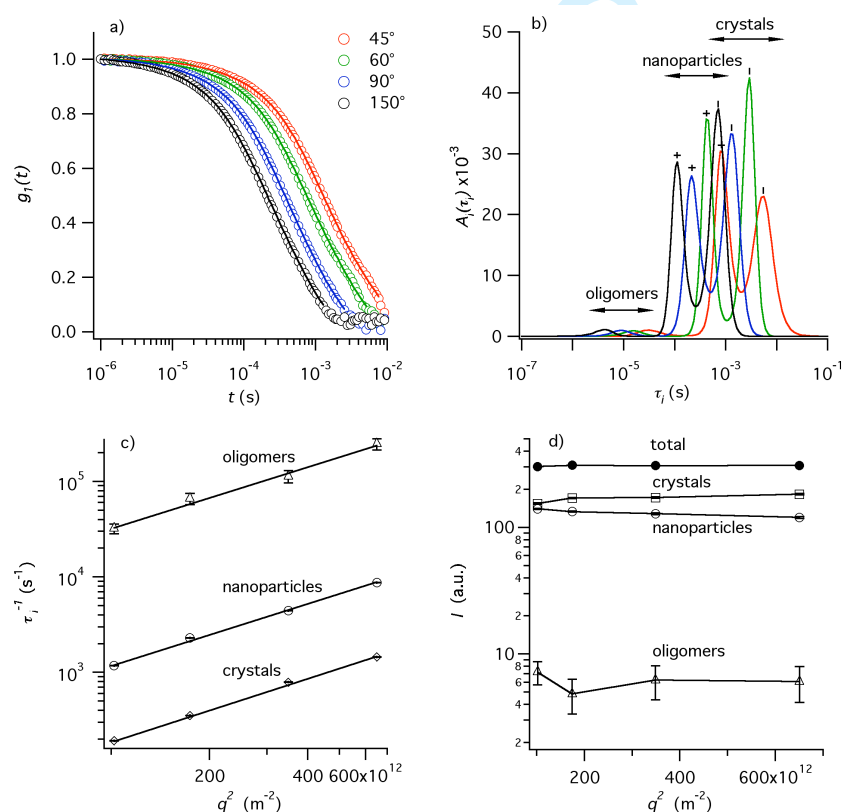


Figure SI-2. Representative light scattering data obtained from the unheated sample of the TPAOH13 series, 8 h after start of dissolution. a) Normalized autocorrelation functions at four scattering angles, b) Corresponding relaxation time distributions. c) Relaxation rates versus q^2 . The slopes of the linear fits

correspond to the diffusion coefficients. d) Contribution of each mode to the total static intensity. Standard deviation error bars were calculated from the peak fitting of the relaxation time distributions.

[§] Berne, B.J.; Pecora, R. *Dynamic Light Scattering*; Dover Publications: New York, 2000; p41, 60.

2.2 Evolution of nanoparticle diameter and static intensity with heating time (TPAOH19 series)

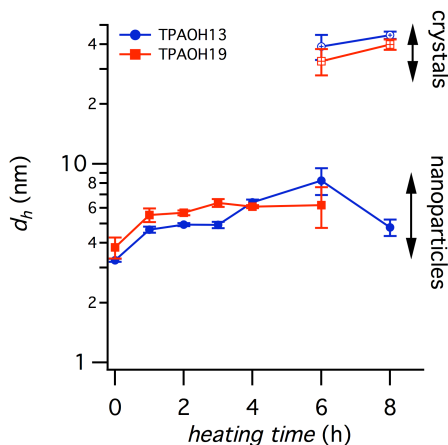


Figure SI-3. Diameter of nanoparticles and crystals versus heating time for TPAOH13 and TPAOH19 series. Each data point was averaged over four scattering angles; error bars represent one standard deviation.

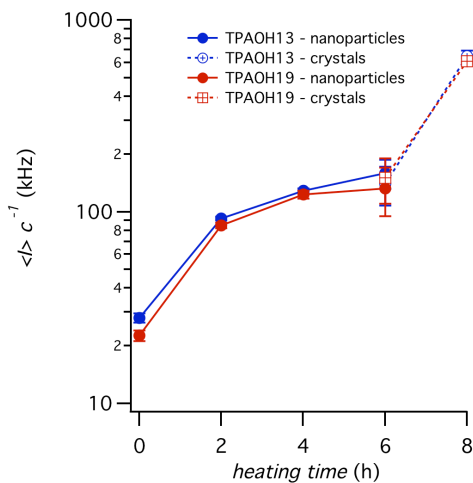


Figure SI-4. Intensity of nanoparticle and crystal modes versus heating time for TPAOH13 and TPAOH19 series. The intensities were scaled with the molar silica concentration. Each data point was averaged over four scattering angles; error bars represent one standard deviation.

2.3 Static intensity of oligomers during dissolution

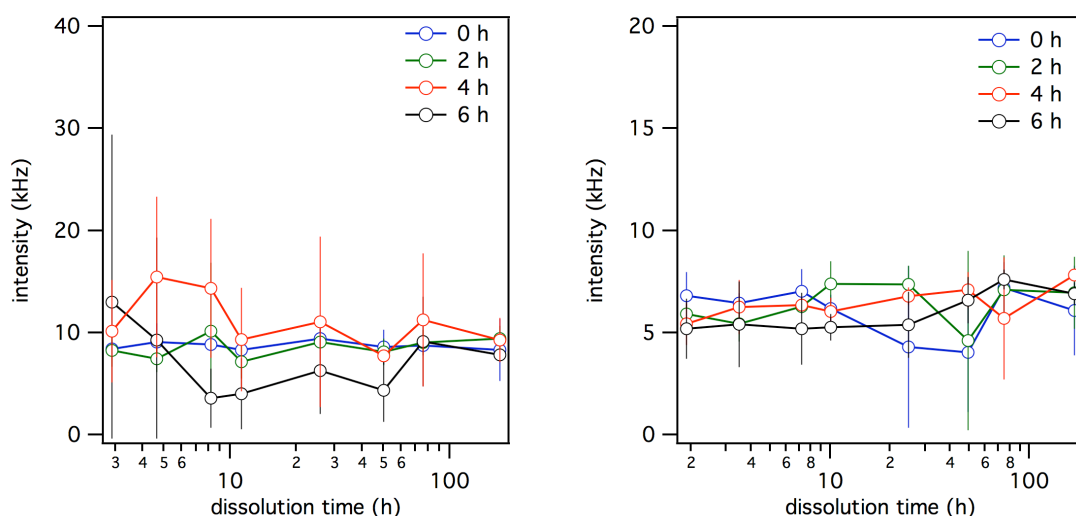


Figure SI-5. Intensity of oligomer mode during dissolution. (left) TPAOH13 series; (right) TPAOH19 series. Each data point was averaged over four scattering angles; error bars represent one standard deviation.

2.4 Reciprocal diffusion coefficients of nanoparticles during dissolution

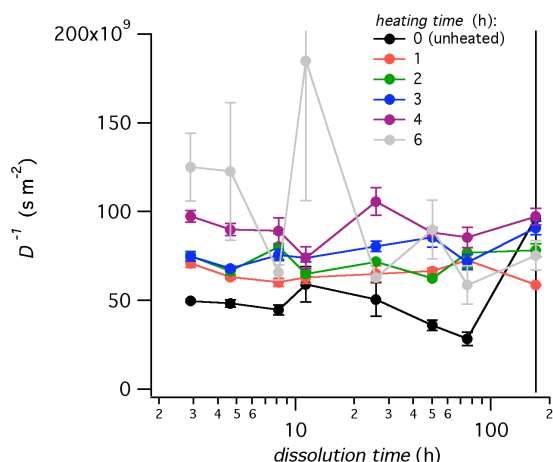


Figure SI-6. Reciprocal diffusion coefficients nanoparticles versus dissolution time, of samples heated between 0 and 8 h before TPAOH addition (TPAOH13 series). Each data point is the average over four scattering angles; error bars represent one standard deviation.

3. SAXS simulations

For each heating time, the pattern after 18-19 h of dissolution was assumed to be equal to the 100 % oligomer pattern, X_{ol} . To retrieve the 100 % nanoparticle pattern X_{np} , a fraction of this 100 % oligomer pattern was subtracted from the pattern after 0.5 h of dissolution, which contains the largest contribution of nanoparticles. The fraction of oligomers was varied until the remaining nanoparticle pattern showed power law decay in the q region $2.5 - 5 \text{ nm}^{-1}$. On a log-log scale, power law decay implies a straight line. Power law decay is typical in this q region, and arises from scattering of the nanoparticle-solvent interface, mass fractal internal structure or specific nanoparticle shape.

After calculation of the 100 % nanoparticle pattern, the weighing factors $a(t)$ in Eq. 2 were determined by minimizing the sum of squared differences between experimental and calculated, composite patterns. The good agreement between simulated and experimental patterns (Figure SI-7) justified the assumption that the system can be described with two varying populations of isolated nanoparticles of constant size and oligomers with constant inter-oligomer spacing.

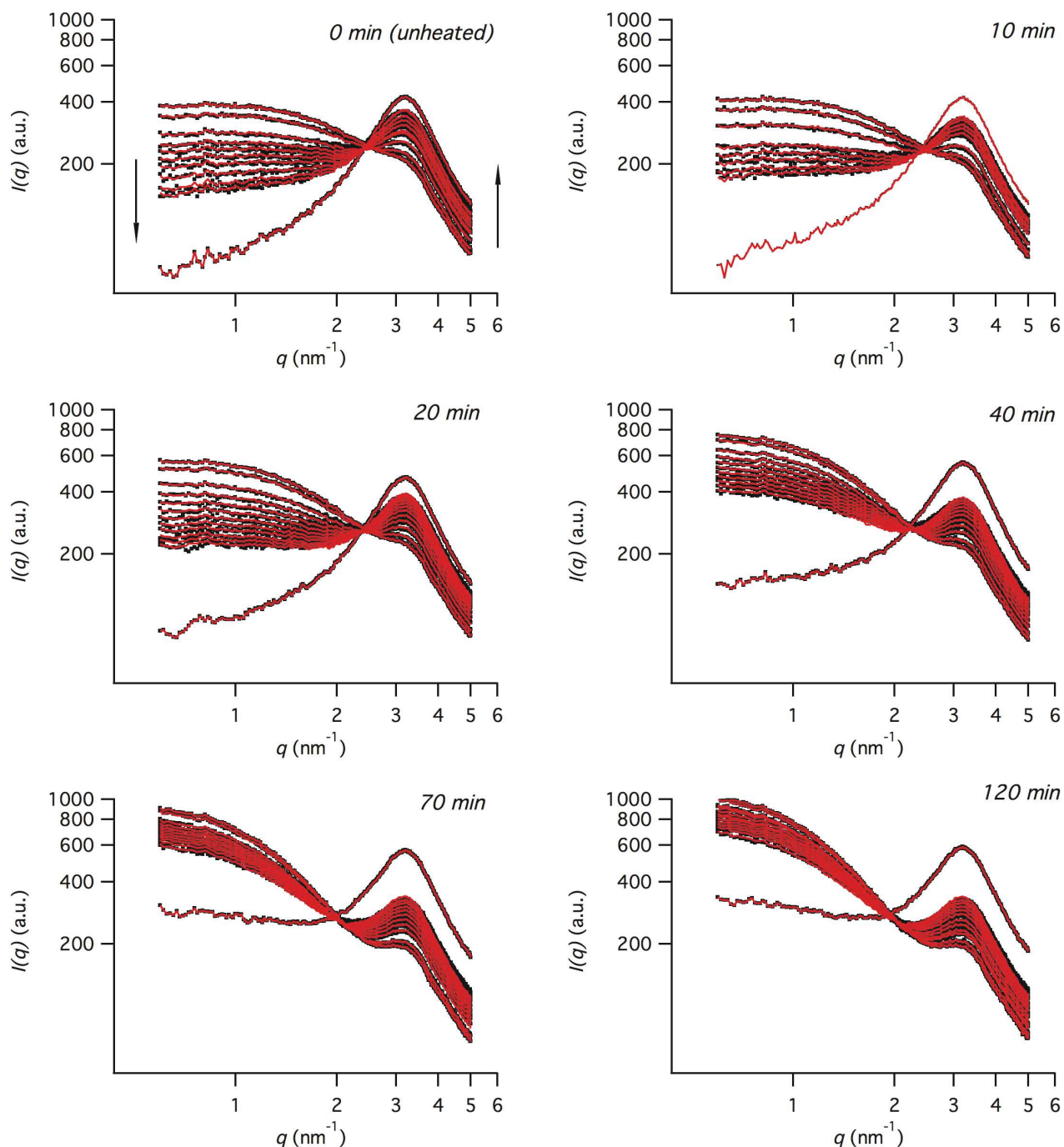


Figure SI-7. Evolution of SAXS patterns with dissolution time of clear sol (TPAOH19 series) heated for 10 minutes to two hours. Black markers: experimental data. The arrows indicate the direction of dissolution time (between 0.5 and 19 h). The thin red curves superimposed on the markers are the simulated patterns.

4. Derivation of equation 3

In Ref [47] the following set of recursive relations were derived for the reaction rate of diffusive transitions over a large free energy barrier consisting of a discrete set of metastable states

$$\begin{aligned} k_{0,n} &= k_{0,1} T[1 \rightarrow^n] \\ T[1 \rightarrow^j] &= \frac{\tau_{j-1,j} T[1 \rightarrow^{j-1}]}{\tau_{j-1,j} + \tau_{j-1,j-2} T[j-2 \rightarrow^0_{j-1}]} \\ T[j-1 \rightarrow^0_j] &= \frac{\tau_{j-1,j-2} T[j-2 \rightarrow^0_{j-1}]}{\tau_{j-1,j} + \tau_{j-1,j-2} T[j-2 \rightarrow^0_{j-1}]} \end{aligned} \quad \text{Eq. SI-5}$$

τ_{jj+1} and $T[1 \rightarrow^j]$ have been explained in the main text of the article. τ_{jj-1} and $T[j \rightarrow^0_{j-1}]$ are similar probabilities for the backward transitions. $\tau_{jj-1} = 1 - \tau_{jj+1}$ and $T[j \rightarrow^0_{j-1}]$ is probability that a sequence of hopping transitions starting from M_j will first visit M_0 before M_{j-1} .

Bringing $T[j-2 \rightarrow^0_{j-1}]$ in front of Eq. SI-5 gives

$$T[j-2 \rightarrow^0_{j-1}] = \frac{\tau_{j-1,j} (T[1 \rightarrow^{j-1}] - T[1 \rightarrow^j])}{(1 - \tau_{j-1,j}) T[1 \rightarrow^j]} \quad \text{Eq. SI-6}$$

or

$$T[j-1 \rightarrow^0_j] = \frac{\tau_{j,j+1} (T[1 \rightarrow^j] - T[1 \rightarrow^{j+1}])}{(1 - \tau_{j,j+1}) T[1 \rightarrow^{j+1}]} \quad \text{Eq. SI-7}$$

Then, we can write for $T[1 \rightarrow^j]$

$$T[1 \rightarrow^j] = T[1 \rightarrow^{j-1}] T[j-1 \rightarrow^j] = T[1 \rightarrow^{j-1}] (1 - T[j-1 \rightarrow^0_j]) \quad \text{Eq. SI-8}$$

This relation says that the probability to go from M_1 to M_j (before visiting M_0) equals the probability to go from M_1 to M_{j-1} times the probability *not* visiting M_0 to M_j starting from M_{j-1} . Substitution of Eq. SI-7 in Eq. SI-8 gives

$$T[1 \rightarrow^j] = T[1 \rightarrow^{j-1}] \left(1 - \frac{\tau_{j,j+1} (T[1 \rightarrow^j] - T[1 \rightarrow^{j+1}])}{(1 - \tau_{j,j+1}) T[1 \rightarrow^{j+1}]} \right) \quad \text{Eq. SI-9}$$

Now, we can bring $T[1 \rightarrow^{j+1}]$ in front to obtain Eq. 3